

# Extremely efficient photocurrent generation in carbon nanotube photodiodes enabled by a strong axial electric field

Daniel R. McCulley<sup>1</sup>, Mitchell J. Senger<sup>1</sup>, Andrea Bertoni<sup>2</sup>, Vasili Perebeinos<sup>3</sup>, Ethan D. Minot<sup>1\*</sup>

<sup>1</sup>*Department of Physics, Oregon State University, Corvallis, Oregon 97331, USA*

<sup>2</sup>*Istituto Nanoscienze-CNR, Via Campi 213a, I-41125 Modena, Italy*

<sup>3</sup>*Department of Electrical Engineering, University at Buffalo, The State University of New York, Buffalo, NY 14260, USA*

## Abstract

Carbon nanotube (CNT) photodiodes have potential to convert light into electrical current with high efficiency. However, previous experiments have revealed photocurrent quantum yield (PCQY) well below 100%. In this work, we show that axial electric field increases the PCQY of CNT photodiodes. In optimal conditions our data suggest PCQY > 100%. We studied, both experimentally and theoretically, CNT photodiodes at room temperature using optical excitation corresponding to the  $S_{22}$ ,  $S_{33}$  and  $S_{44}$  exciton resonances. The axial electric field inside the pn junction was controlled using split gates that are capacitively coupled to the suspended CNT. Our results give new insight into the photocurrent generation pathways in CNTs, and the field dependence and diameter dependence of PCQY.

Keywords: carbon nanotube, exciton dissociation, carrier multiplication, scanning photocurrent microscopy

## Main Text

The performance of optoelectronic devices depends critically on the relaxation pathways available to energetic charge carriers. In nanomaterials, these relaxation pathways can differ dramatically from traditional bulk semiconductors. For example, substantial effort has focused on engineering multiple exciton generation pathways in quantum dots (QDs) to optimize performance for photovoltaic cells.<sup>1-5</sup> Advances in QD device design have led to the experimental realization of internal quantum efficiency greater than 100% when  $\hbar\omega \gtrsim 3E_g$  where  $E_g$  is the band gap of the light-absorbing material.<sup>6-8</sup>

Carbon nanotubes offer unique relaxation pathways for energetic charge carriers.<sup>9</sup> These key pathways arise because of the one-dimensional band structure of CNTs and the strong Coulomb interactions between the charge carriers. The energy scale for Coulomb interactions in CNTs is remarkably large:  $e^2/4\pi\epsilon_{\text{eff}}D$  is of the order hundreds of meV, where  $D$  is the CNT diameter,  $e$  is the electron charge and  $\epsilon_{\text{eff}}$  is the effective dielectric constant. The strong Coulomb interaction enables relaxation mechanisms such as impact ionization which can potentially boost the quantum efficiency of the photodiode.<sup>10,11</sup>

In 2009, Gabor et al. found signatures of multiple electron-hole generation in the photocurrent from CNT photodiodes at temperatures below 60 K.<sup>12</sup> Significantly, the signature of multiple electron-hole generation was apparent at the CNT's second optical resonance ( $\hbar\omega \sim 2E_g$ ). However, the authors did not quantify photocurrent quantum yield (PCQY). Photocurrent quantum yield is defined here as the number of electrons extracted as the photocurrent divided by the number of photons absorbed by the intrinsic region of the CNT p-i-n junction.

Later experiments on CNTs found multiple exciton generation at room temperature when  $\hbar\omega \approx 3E_g$ .<sup>13</sup> In that work, the optical technique was sensitive to excitons, but not sensitive to photocurrent.<sup>13</sup> Early photocurrent measurements estimated the external quantum efficiency of CNT photodiodes.<sup>14</sup> The first optoelectronic measurement that quantified PCQY in a CNT photodiode found  $\sim 3\%$ .<sup>15</sup> In that work, the CNT photodiode was excited at the first and second optical resonances ( $S_{11}$  and  $S_{22}$  resonance). Aspirtarte et al. used a different device geometry, and  $\hbar\omega > 4E_g$  to show room-temperature PCQY  $\sim 30\%$  ( $S_{44}$  and  $S_{55}$  optical resonances).<sup>16</sup> Using a third device geometry, barrier-free bipolar CNT diodes, Wang et al. estimated room-temperature PCQY as high as  $\sim 60\%$  at the  $S_{11}$  optical resonance.<sup>17</sup> Lastly, Kumamoto et al. used a combination of photocurrent and photoluminescence from a suspended CNT under high bias (no pn junction) to estimate PCQY  $\sim 60\%$  at an electric field  $\sim 15$  V/ $\mu\text{m}$  (excitation at the  $S_{22}$  resonance).<sup>18</sup> The experiments by Wang et al.<sup>17</sup> and Kumamoto et al.<sup>18</sup> suggest large axial electric field is critical to achieving high PCQY in CNT photodiodes. Indeed, theory predicts a significant increase in PCQY when axial field becomes strong enough to enable exciton dissociation and impact ionization.<sup>19,20</sup>

Here, we quantify PCQY in CNT photodiodes while varying electric fields from 2 V/ $\mu\text{m}$  up to 15 V/ $\mu\text{m}$ . Our devices are similar to those built by Chang et al. who reached 2 V/ $\mu\text{m}$ ,<sup>21,22</sup> and Aspirtarte et al. who reached 4 V/ $\mu\text{m}$ .<sup>16</sup> We determine PCQY using a model that accounts for the length of the intrinsic region inside the CNT photodiode, optical cavity effects, and the integrated absorption cross-section of the exciton resonances. At low fields we confirm previous estimates

of PCQY, and at high fields our data suggest PCQY > 100% at the  $S_{22}$  optical resonance ( $\hbar\omega \sim 2E_g$ ).

The design of our CNT photodiode device is shown schematically in Figure 1a. A single carbon nanotube is suspended between platinum source and drain electrodes. The source and drain electrodes are separated by a trench that is 0.65  $\mu\text{m}$  deep and 2.6  $\mu\text{m}$  wide. At the bottom of the trench are two gate electrodes separated by a 500 nm gap and covered in 50 nm of  $\text{SiO}_2$ . The suspended CNTs are grown over the trench by a fast-heat chemical vapor deposition process as the final fabrication step. The CNTs are grown at 800  $^\circ\text{C}$  using an iron catalyst and a mixture of methanol/ethanol vapor mixed with Ar and  $\text{H}_2$  (see Supporting Information for further details).<sup>23</sup> This fabrication method ensures that the CNTs are never exposed to photoresist or other processing chemicals.<sup>9–11</sup>

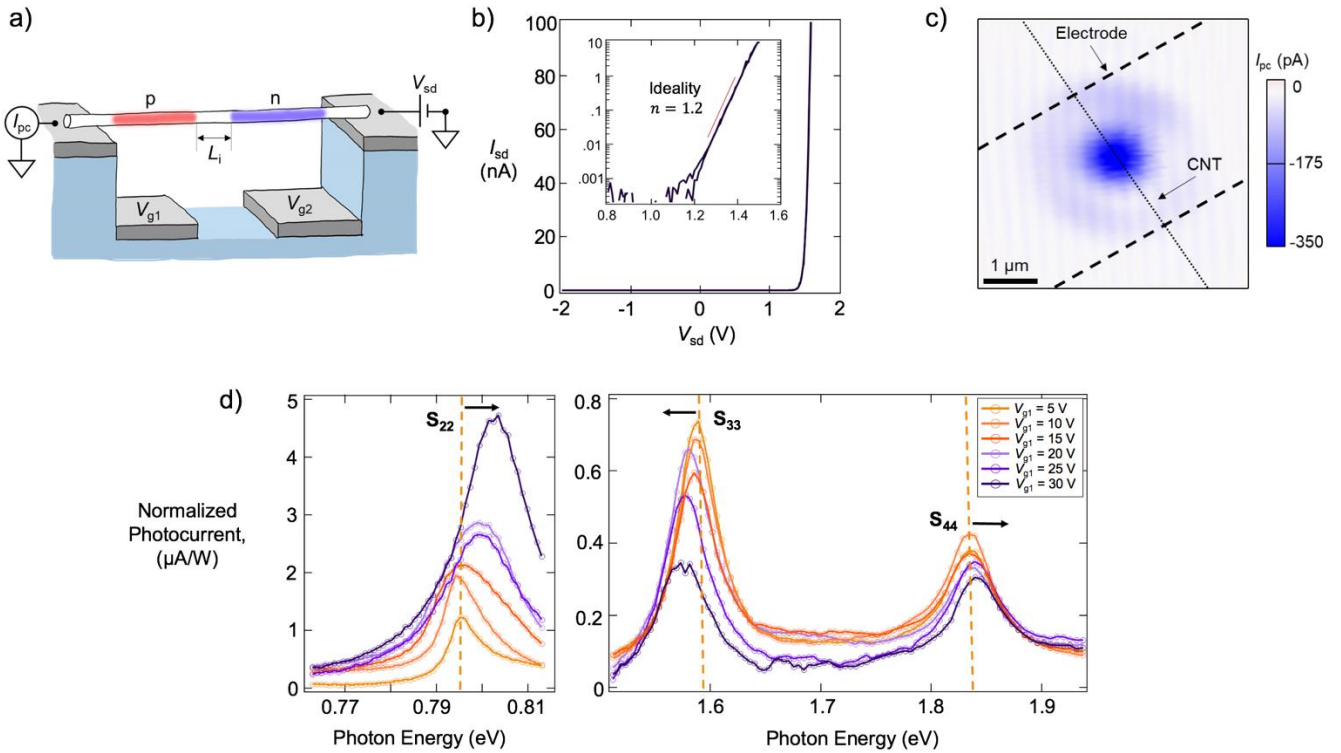


**Figure 1.** **a)** Schematic of CNT electrode configuration. **b)** Dark  $I$ - $V_{sd}$  curve of a suspended carbon nanotube p-n junction with  $V_{g2} = -V_{g1} = 5$  V. **c)** Scanning photocurrent image of a CNT photodiode. **d)** Power normalized photocurrent spectrum around the  $S_{22}$ ,  $S_{33}$ , and  $S_{44}$  exciton resonances of a CNT with chiral index (22,14) and diameter = 2.46 nm. The spectrum was obtained with  $V_{sd} = -0.5$  V and optical power  $\sim 10$   $\mu\text{W}$  spread over an area  $\sim 100$   $\mu\text{m}^2$ .

The suspended CNT is operated as a photodiode by applying a negative voltage to the left gate ( $V_{g1}$ ) and a positive voltage to the right gate ( $V_{g2}$ ), as shown in Fig. 1a. The left side of the

CNT is coupled electrostatically to the left gate, so this half of the CNT becomes p-doped. Similarly, the right half of the CNT becomes n-doped. An intrinsic region of length  $L_i$  lies between the p-doped region and the n-doped region. The axial electric field in this intrinsic region is controlled by the gate voltages  $V_{g1} = -V_{g2}$ . All experiments described here are performed at room temperature in a vacuum environment unless otherwise stated.

Figure 1b shows the dark  $I$ - $V_{sd}$  characteristics of a CNT diode device. As reported previously,<sup>16,24,25</sup> we observe rectifying behavior in reverse bias and an exponential turn-on in forward bias with ideality factor in the range 1.05 – 1.32.

Figure 1c shows a photocurrent image of the CNT photodiode. The image is taken by focusing the laser and raster scanning the surface. The photocurrent is recorded as a function of laser position. Photocurrent is only generated in the intrinsic region at the center of the CNT. Optical excitation of the p-doped and n-doped region does not lead to photocurrent because non-radiative decay processes cause rapid recombination of electron-hole pairs in the doped regions.<sup>26,27</sup>

A representative set of photocurrent spectra are shown in Fig. 1d. The photocurrent is generated using a defocused laser spot with an intensity of approximately 10 W/cm<sup>2</sup>. The optical intensity is sufficiently low that photocurrent is linear with respect to laser power (Supporting Figure S3a). The light source is a supercontinuum laser with 320 MHz pulse rate (NKT Photonics). White light from the supercontinuum is filtered by a double monochromator to give monochromatic light with a 5 nm bandwidth.<sup>28</sup> A reverse bias is applied to the photodiode ( $V_{sd} = -0.5$  V). The photocurrent and optical power are monitored simultaneously to allow accurate power normalization. The spectral peaks seen in Fig. 1d are associated with excitonic resonances.<sup>29</sup> The peak positions are compared with an atlas of CNT optical properties<sup>30</sup> and are used to identify the chiral index.<sup>31</sup>

Photocurrent spectra were measured at various split-gate voltages (Fig. 1d). As the split-gate voltage increases, the  $S_{22}$  peak is blue shifted, the  $S_{33}$  peak is red shifted, and the  $S_{44}$  peak is blue shifted. The magnitudes of the shifts are higher than expected from the Stark effect (see Supporting Information). Shifts of alternating sign are consistent with axial strain from the electrostatic force pulling the CNT towards the gates. Comparing the measured peak shifts to previous studies of strained CNTs,<sup>32,33</sup> we estimate that axial strain reaches ~ 0.2%. This voltage-controlled tuning of optical resonances is an interesting effect, and potentially useful for CNT-based quantum-light sources.<sup>34</sup> However, the effect is not central to the main focus of our paper.

We are interested in quantifying PCQY as we increase the split-gate voltages (i.e. strengthen the axial electric field in the center of the CNT). Therefore, we calculated the integrated area of each photocurrent peak in Fig. 1d. The  $S_{22}$  photocurrent peak area increases by a factor of 6.5. In contrast, the  $S_{33}$  and  $S_{44}$  peak areas decrease by a factor of 2.2 and 1.4 respectively. The peak areas depend on a number of factors, one of which is PCQY, as explained below.

To understand the factors contributing to peak area (Fig. 1d), consider the integral of the  $i^{\text{th}}$  photocurrent peak,

$$\int_{S_{ii}} I_{\text{pc}} d(\hbar\omega) = e \cdot \eta_{ii} \cdot \Phi \cdot L_i \cdot N_L \int_{S_{ii}} \sigma_c d(\hbar\omega), \quad (1)$$

where  $e$  is the electron charge,  $\eta_{ii}$  is the PCQY at the  $i^{\text{th}}$  exciton resonance,  $\Phi$  is the photon flux,  $L_i$  is the intrinsic region length,  $N_L$  is the number of atoms per length on the nanotube,  $\sigma_c$  is the absorption cross-section per carbon atom, and  $\int \sigma_c d(\hbar\omega)$  is the oscillator strength per carbon atom. The product  $(N_L \cdot \int \sigma_c d(\hbar\omega))$  can be found from the chiral index of the CNT.<sup>35</sup> The experimental variables  $\Phi$  and  $L_i$  must be carefully characterized if one wishes to determine  $\eta_{ii}$ .

We first describe our method to characterize the intrinsic region length,  $L_i$ . At low electric field,  $L_i$  can be directly imaged.<sup>16</sup> At high field, however,  $L_i$  is smaller than the point spread function of the laser spot. Therefore, we used self-consistent electrostatic-field (SCF) calculations to find the relationship between the  $V_{g1}$ ,  $V_{g2}$ ,  $V_{sd}$ , and  $L_i$ . Details of the simulations are given in the Supporting Information. Briefly, in the first step of calculation, we find electrostatic potential field without any CNT connecting the source and drain electrodes. The voltages on the four electrodes and the cross-sectional geometry of the device (Fig. 2a) define the electrostatic boundary conditions. The 2-d electrostatic potential field is calculated using a relaxation algorithm to solve the Laplace equation. From this zeroth-order solution, we obtain a first estimate of the electric field at the center of the pn junction (grey dashed line in Fig. 2d). In the next step of calculation, the CNT is populated with charge and an effective 1-d mean-field simulation is used to refine the results of the electrostatic potential model. This step is repeated many times until a self-consistent solution is reached. The final result includes the charge density along the length of the CNT (Fig. 2b), the band bending diagram (Fig. 2c), and the electric field at the center of the CNT (open circles in Fig. 2d).

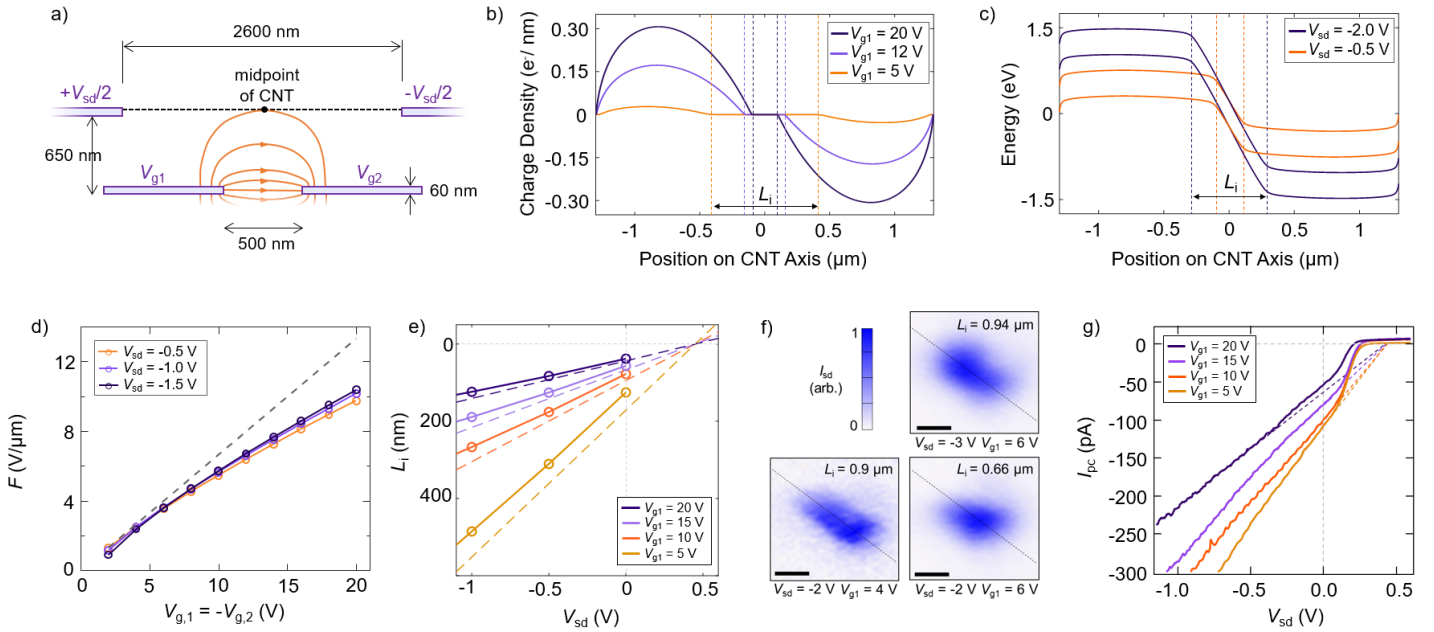


**Figure 2.** **a)** Schematic of the geometry used in the self-consistent electrostatic-field (SCF) calculations. Electric field lines are sketched in orange. **b)** Calculated charge density along the length of a CNT with  $E_g = 0.45$  eV. The gate voltages are equal and opposite ( $V_{g1} = -V_{g2}$ ). All three curves are calculated with  $V_{sd} = 0$ . **c)** Calculated band bending diagram (the edge of the valance and conduction bands) when  $V_{g1} = -V_{g2} = 6$  V and  $E_g = 0.5$  eV. **d)** The axial-component of electric field at the center of the CNT. The grey dashed line shows the result of a zeroth-order calculation (assuming no charge on the CNT). Open circles show the results of the SCF calculations. **e)** Open circles show the calculated value of the intrinsic region length,  $L_i$ . The dashed lines shows values of  $L_i$  estimated using Eq. 2. **f)** Scanning photocurrent images showing elongation of the intrinsic region when  $|V_{sd}|$  increases or  $V_{g1} = -V_{g2}$  decreases. The scale bar is  $0.5 \mu\text{m}$ . Dashed lines indicate the CNT axis. **g)** Experimental measurement of photocurrent for a (20,16) CNT excited at the  $S_{44}$  resonance ( $\hbar\omega = 1.92$  eV). Photocurrent grows linearly with  $V_{sd}$  when for  $V_{sd} < 0$ . Linear extrapolations of these curves intercept the x-axis at the  $V_{sd} = 0.4$  V, corresponding to the expected band gap of this CNT.

Figure 2b shows the charge density along the nanotube for different split gate voltages. The region of near-zero charge in the center of the CNT corresponds to the intrinsic region. To measure the length of the intrinsic region,  $L_i$ , we set an upper limit for the charge density in the intrinsic region of  $0.001 e \text{ nm}^{-1}$  (see Supporting Information for further discussion of the charge density cut-off parameter). The length of the intrinsic region decreases as the split-gate voltages increase. Figure 2c shows band bending diagrams for different values of  $V_{sd}$ . The slope of the band edges in Fig. 2c correspond to the axial electric field. The field in the center of the CNT,  $F$ ,

is primarily determined by  $V_{g1} = -V_{g2}$ . Note that  $F$  is almost unaffected by the typical  $V_{sd}$  voltages used in our experiment; the main effect of  $V_{sd} < 0$  is to lengthen  $L_i$ . In summary, the results of the self-consistent field calculations are well described by the relationship

$$L_i \approx \frac{|V_{sd} - E_g/e|}{F} \quad \text{when } V_{sd} < 0, \quad (2)$$

where  $E_g$  is the band gap of the CNT. Equation 2 is plotted in Fig. 2e (dashed lines) and compared to the results of the SCF calculation (open circles). We used scanning photocurrent microscopy to confirm that  $L_i$  changes as expected with respect to  $V_{sd}$  and the split-gate voltages (see Fig. 2f and additional images/analysis in Supporting Information). The good agreement between Eq. 2 and the measured values of  $L_i$  give us additional confidence in the electrostatics modeling.

Recalling that  $I_{pc} \propto L_i$  when  $\eta_{ii}$  is held constant (Eq. 1), we note that measurements of  $I_{pc}$  vs.  $V_{sd}$  can also be used to check our model for  $L_i$ . We confirmed that  $I_{pc}$  grows linearly with  $V_{sd}$  when  $V_{sd} < 0$  (Fig. 2g). We also confirmed that  $dI_{pc}/dV_{sd}$  is modified by changing  $F$ , and confirmed that  $I_{pc}(V_{sd})$  extrapolates to an  $x$  intercept that is consistent with the expected value of  $E_g$  (Fig. 2g).

To complete our analysis of the factors in Eq. 1, consider the photon flux,  $\Phi$ , given by

$$\Phi = \frac{P_0 \cdot \beta}{\hbar\omega \cdot A_{spot}} \quad (3)$$

where  $P_0$  is the laser power,  $\beta$  is a power enhancement factor (caused by light reflecting from the substrate) and  $A_{spot}$  is the effective area of the Gaussian point spread function.  $\beta$  is calculated using finite difference time domain (FDTD) simulations performed on commercially available software (Lumerical). The simulations account for the wavelength-dependence of the reflection coefficient, and interference effects (destructive or constructive). The power enhancement factor,  $\beta$ , varies from 0.2 to 2.7 across the full spectral range the laser. At a given wavelength,  $\beta$  depends on the exact height of the CNT above the split gates. An uncertainty in height of  $\pm 10$  nm leads to uncertainty in  $\beta$  of no more than  $\pm 10\%$ . The effective area of the laser spot,  $A_{spot}$ , is determined from photocurrent imaging. A more detailed discussion of  $\beta$  and  $A_{spot}$  is provided in the Supporting Information.

In Fig. 3 we illustrate how Eq. 1 is applied to  $I_{pc}(\hbar\omega)$  measurements to determine the field dependence of PCQY. The CNT diameter is 2.51 nm and the photon energy is scanned over the  $S_{33}$  resonance ( $\hbar\omega \approx 4E_g$ ). First, the photocurrent spectra were measured at various values of  $V_{g1} = -V_{g2}$  (Figure 3a) with a small reverse bias applied to the device ( $V_{sd} = -0.5$  V). Next, SCF

simulations were used to find  $L_i$  (Fig. 3b) and the photocurrent data was divided by  $e \cdot \Phi \cdot L_i$  (Fig. 3c). Last, we integrated the peaks in Fig. 3c and compared with the expected oscillator strength per unit length,  $N_L \int_{S_{33}} \sigma_c d(\hbar\omega)$ . For this CNT chirality  $N_L = 307.1$  atoms/nm and  $\int_{S_{33}} \sigma_c d(\hbar\omega) = 1.63 \times 10^{-18} \text{eV cm}^2$  (further discussion of oscillator strength is provided in the Supporting Information). The PCQY is then given by

$$\eta_{33} = \int_{S_{33}} \frac{I_{pc}(\hbar\omega)}{e \cdot \Phi \cdot L_i} d(\hbar\omega) / \left( N_L \int_{S_{33}} \sigma_c d(\hbar\omega) \right). \quad (4)$$

These  $\eta_{33}$  values are plotted in Fig. 3d.

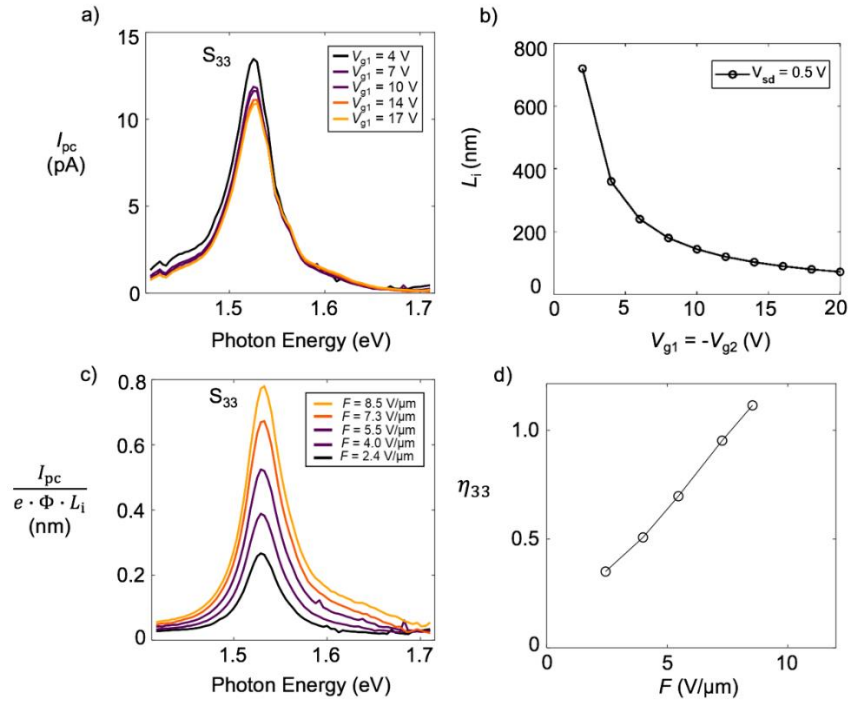


**Figure 3.** **a)** The photocurrent spectrum at increasing gate voltage centered on the  $S_{33}$  exciton resonance of a (19,18) CNT with a diameter of 2.51 nm.  $V_{sd} = -0.5$  V. **b)** The intrinsic region length at increasing gate voltage. **c)** The photocurrent spectrum normalized by the photon flux and intrinsic region length. The optical intensity is  $\sim 0.7 \mu\text{W}/\mu\text{m}^2$  at  $\hbar\omega = S_{33}$ . For the optical excitation spectrum see Supporting Information Device J Summary). **d)** The photocurrent quantum yield,  $\eta_{33}$ , as a function of axial electric field,  $F$ .

The PCQY at low field ( $\eta_{33} \approx 35\%$ ) is similar to previously reported PCQY at  $S_{44}$  and  $S_{55}$  exciton resonances.<sup>16</sup> As the field increases from 2.4 V/ $\mu\text{m}$  to 8.5 V/ $\mu\text{m}$ , however,  $\eta_{33}$  increases

by more than a factor of 3 and begins to exceed 100% PCQY. The upward trend in  $\eta_{33}(F)$  suggests that even higher values of  $\eta_{33}$  would be possible if our device could sustain larger split gate voltages. This result suggests that room temperature carrier multiplication can be achieved when  $\hbar\omega \approx 4E_g$ .

For efficient light-harvesting applications, the most intriguing possibility is carrier multiplication when  $\hbar\omega \approx 2E_g$ . Therefore, we now focus on measurement of  $\eta_{22}(F)$ . We have studied the  $S_{22}$  resonance of 8 different CNTs. The CNT diameters range from 2.0 to 2.9 nm (the  $S_{22}$  energies range from 1.05 to 0.72 eV). As the split gate voltage is increased, we track the spectral position of the  $S_{22}$  peak. The peaks shift upward or downward in energy depending on the interplay between axial strain and CNT band structure.<sup>33</sup> We independently verified the CNT “family index” by performing chiral index assignment. Six CNTs are from the family  $(n - m) \bmod 3 = 1$ , and two CNTs are from the family  $(n - m) \bmod 3 = 2$  (see Fig. 4a). The family index correctly predicts the direction of the peak shift.

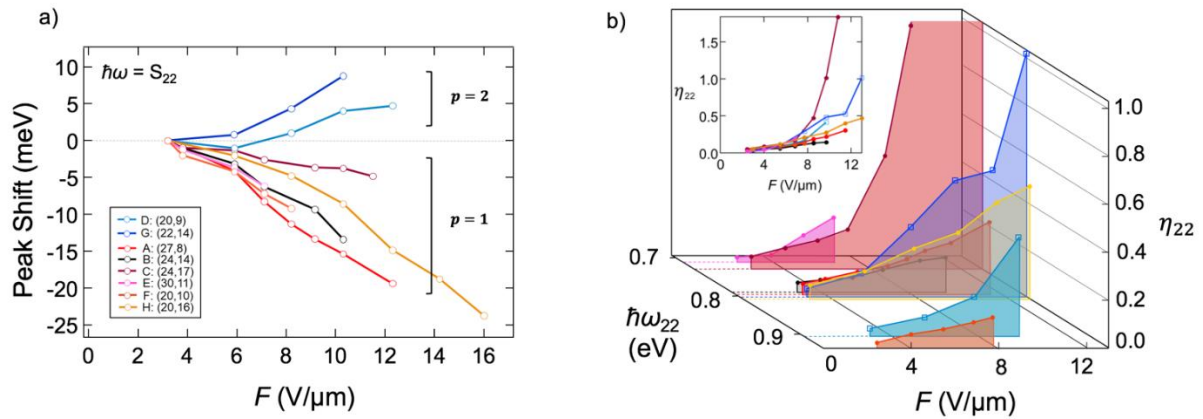


**Figure 4. a)**  $S_{22}$  peak position as a function of axial electric field for eight different CNTs with known chirality. **b)** The photocurrent quantum yield at the  $S_{22}$  exciton resonance for 8 different CNTs as a function of increasing axial electric field.  $V_{sd} = -0.5$  V. Squares indicate insufficient data to determine photon flux.

For each CNT, we measured  $I_{pc}(\hbar\omega)$  and divided the spectra by  $e \cdot \Phi \cdot L_i$  (see Supporting Information Fig. S12 – S29). The integrated spectral peaks were then compared with the expected oscillator strength per unit length,  $N_L \int_{S_{22}} \sigma_c d(\hbar\omega)$ . The resulting values of  $\eta_{22}$  are plotted in Fig. 4b. The  $\eta_{22}(F)$  curves have been sorted by  $\hbar\omega_{22}$  (the photon energy corresponding to  $S_{22}$  at low  $F$ ). When interpreting Fig. 4, the  $\hbar\omega_{22}$  axis can be used as proxy for CNT diameter ( $\hbar\omega_{22} \propto 1/D$ ) or exciton binding energy ( $\hbar\omega_{22} \propto E_b$ ). We find the largest values of  $\eta_{22}$  when  $\hbar\omega_{22}$  is small.

At low  $F$ ,  $\eta_{22} = 0.03 - 0.05$ , in agreement with previous measurements of  $\eta_{22}$ .<sup>15</sup> In the smallest diameter CNTs (large  $\hbar\omega_{22}$ ), we find that  $\eta_{22}$  increases modestly with  $F$ . In the larger diameter CNTs (smaller  $\hbar\omega_{22}$ ), however, we find that  $\eta_{22}$  increases as much as 35-fold. One device exhibits  $\eta_{22} = 1.7$  (see Figure 4b and Supporting Figure S16). All curves get steeper at high field suggesting that  $\eta_{22}$  would increase further if our devices could sustain higher split-gate voltages.

The calibration process to quantify PCQY has multiple steps and we have attempted to crosscheck the process as much as possible. First, we note that low-field PCQY agrees with previous work.<sup>15 16</sup> Second, when photocurrent spectra are normalized by  $\beta$ , the resonance line shapes match the expected Lorentzian line shape. Third, our model for  $L_i$  was verified by photocurrent imaging and by measuring  $I_{pc}$  vs.  $V_{sd}$  (Fig. 2f & g). Fourth, we crosschecked the calculated values of  $F$  by comparing the average spectral shift (Fig. 4a) to the expected Stark shift of  $S_{22}$  resonances (see SI). Overall, we estimate that our calibration process yields PCQY values with  $\sim\pm 30\%$  uncertainty. An additional source of uncertainty, which we cannot mitigate with our experimental design, is uncertainty in the integrated absorption cross-section

$\int_{S_{ii}} \sigma_c d(\hbar\omega)$ . Liu et al. measured  $\int_{S_{ii}} \sigma_c d(\hbar\omega)$  for more than 50 individual suspended CNTs.<sup>35</sup> Their measured values were distributed above/below the line of best fit by  $\sim \pm 30\%$ . We used Liu's line of best fit for our analysis, thus the overall uncertainty in our PCQY determination is  $\sim \pm 40\%$ . We note there is significantly less uncertainty associated with our measurements of the *relative* change in PCQY as a function of  $F$  for a particular CNT.

To interpret our measurements of PCQY, we consider the relaxation pathways of  $S_{22}$  and  $S_{33}$  excitons, and the expected field-dependence of these pathways (Fig. 5). First, consider the relaxation of the  $S_{22}$  excitons when  $F$  is too small to induce exciton dissociation. In this low-field regime,  $\eta_{22}$  increases almost linearly with  $F$  (see Fig. 4b). Kumamoto et al. studied this regime in detail and proposed that free carriers are produced by spontaneous dissociation of  $S_{22}$  excitons (Fig. 5a). These free carriers are then converted to photocurrent if the electric field sweeps out the free carriers faster than they form bound states.<sup>18</sup> We have verified that Kumamoto's model is applicable to our system by calculating the decay products for spontaneous dissociation of  $S_{22}$  excitons in an experimentally relevant CNT (Fig. 5b). Spontaneous dissociation occurs via either an electronic pathway or a phonon-mediated pathway, with a branching ratio  $\sim 1:10$  (the phonon pathway is about 10 times more probable).<sup>36</sup> The electronic pathway produces only free e-h pairs ( $e_1 + h_1$ ).<sup>36,37</sup> The phonon-mediated pathway produces a variety of products: free e-h pairs ( $e_1 + h_1$ ,  $e_2 + h_1$ ,  $e_1 + h_2$ ), bound, and

partially bound excitons.<sup>36,37</sup> We solved the Bethe-Salpeter equation for the phonon decay mechanism.<sup>36,37</sup> Our calculations for the experimentally relevant (20,9) CNT show that most of the products of the phonon-mediated  $S_{22}$  decay pathway have electron-hole separation greater than the bound  $S_{11}$  or  $S_{12}$  exciton radiuses i.e.  $\gg 2$  nm (Fig. 5b).

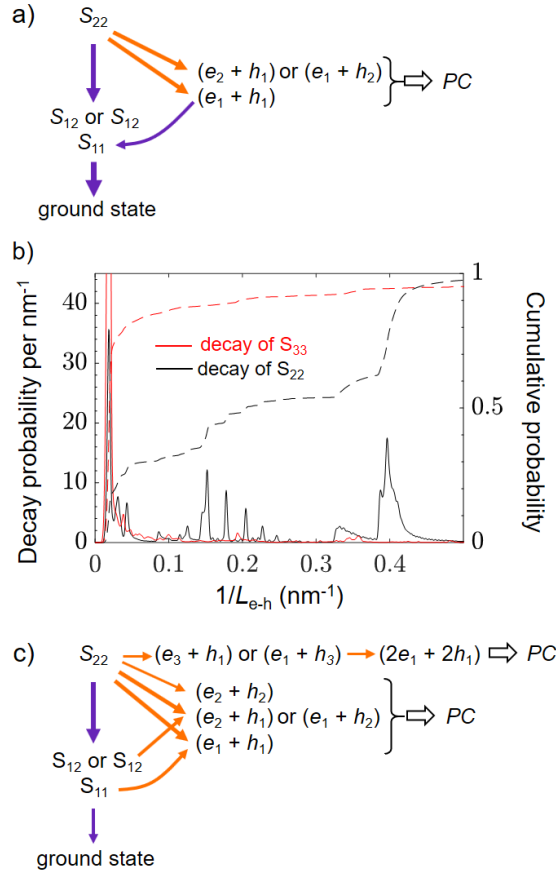


**Figure 5. a)** Proposed pathways for relaxation of the  $S_{22}$  exciton at low field (no field-induced exciton dissociation). Pathways that can lead to photocurrent (PC) are shown in orange. White arrows represent free carriers that are swept out by electric field. **b)** Computational modeling of a (20, 9) CNT. The model calculates the size distribution of the e-h separation of the decay products of the  $S_{22}$  and  $S_{33}$  phonon decay mechanism. The x-axis is the inverse size of the e-h separation using a two-particle wavefunction from the Bethe-Salpeter Equation solution. Solid lines represent the probability of generating the decay product with a certain e-h separation, and dashed lines represent the cumulative probability. The leftmost peaks in probability correspond to free carriers ( $L_{e-h} = 50$  nm = one quarter of the length of the simulated supercell). The rightmost peak for  $S_{22}$  decay (about 40% of the total decay products) corresponds to fully bound  $S_{11}$  and  $S_{12}$  excitons ( $L_{e-h} \approx 2.5$  nm). **c)** Possible relaxation pathways of the  $S_{22}$  exciton at high field, including field-induced dissociation of  $S_{11}$ ,  $S_{12}$ ,  $S_{21}$  and  $S_{22}$  excitons.

If  $S_{22}$  decay products are not swept out of the intrinsic region, they will likely reach the  $S_{11}$  exciton state. At low field, the  $S_{11}$  exciton can undergo either radiative recombination ( $\tau_{\text{rad}} \sim 10$  ns<sup>26,38,39</sup>) or non-radiative recombination. To estimate the non-radiative recombination time in our system,  $\tau_{\text{non-rad}}$ , we assume that excitons diffuse to the ends of the intrinsic region where end quenching occurs.<sup>27,40</sup> The typical length of the intrinsic region is  $L_i \approx 100$  nm, and the exciton diffusion constant is approximately  $10$  cm<sup>2</sup>/s,<sup>41</sup> therefore,  $\tau_{\text{non-rad}} \approx 10$  ps.

When  $F$  is sufficiently large, field-induced exciton dissociation may occur. There is previous experimental evidence that  $S_{11}$  excitons can be dissociated by large electric fields. In that previous work, electric field was applied perpendicular to the CNT axis.<sup>42</sup> In contrast, our experiment uses axial electric field and carriers are kept inside the CNT. A theoretical description of our system (at the perturbation level) predicts that the  $S_{11}$  dissociation time is given by<sup>19</sup>

$$\tau_{\text{diss}} = \frac{\hbar F}{4E_b F_0} \cdot \exp\left(\frac{F_0}{F}\right) \quad (5)$$

where  $E_b$  is the exciton binding energy and  $F_0$  is a characteristic field which scales with  $E_b$ . For our CNT diameters,  $E_b$  ranges from approximately 130 to 160 meV,<sup>43</sup> and  $F_0$  ranges from approximately 60 to 80 V/ $\mu\text{m}$ .<sup>19</sup>  $S_{11}$  dissociation becomes significant when  $\tau_{\text{diss}}$  is short compared to  $\tau_{\text{non-rad}}$ . Eq. 5 predicts that  $\tau_{\text{diss}} < \tau_{\text{non-rad}}$  when  $F$  exceeds 5 to 10 V/ $\mu\text{m}$  (the field threshold depends on  $E_b$ ). We verified the predictions of Eq. 5 by solving the Bethe-Salpeter equation for an exciton in the presence of a static axial electric field (see SI). Both theoretical approaches are consistent with our experimental observation that  $\eta_{22}$  grows dramatically for larger diameter CNTs when  $F$  exceeds  $\sim 8$  V/ $\mu\text{m}$  (Fig. 4b). We conclude that field-assisted dissociation of  $S_{11}$  can explain much of the observed increase in  $\eta_{22}$ . However, field-assisted dissociation is not sufficient to explain  $\eta_{22} > 1$ .

Our observation that  $\eta_{22}$  may exceed 100% suggests that carrier multiplication can occur at room-temperature in large-diameter suspended CNTs ( $\geq 2.6$  nm) when  $F$  is sufficiently large ( $\geq 10$  V/ $\mu\text{m}$ ). Previous authors have hypothesized that such carrier multiplication can be expected from impact ionization.<sup>12,20</sup> However, it is difficult to reconcile momentum conservation with impact ionization in the second subband of semiconducting CNTs.<sup>11</sup> Our measurements, together with previous evidence,<sup>12</sup> suggest that impact ionization models may have to incorporate phonons (or additional carriers) to describe experiments. The details of  $S_{22}$  decay in

the presence of strong electric field has been the subject of additional theoretical work,<sup>20</sup> and remains an open question. Some possible pathways are illustrated in Fig. 5c.

Photocurrent quantum yield from the  $S_{33}$  exciton (Fig. 3d) exhibits a different field dependence than PCQY from  $S_{22}$ . At low field,  $\eta_{33}$  is significantly higher than  $\eta_{22}$  (~ 30% compared to 5%) which may be explained by the spontaneous decay products of  $S_{33}$ . Figure 5b shows that almost 100% of the products from the phonon-mediated  $S_{33}$  decay pathway are free carriers. The electronic pathway for spontaneous dissociation of  $S_{33}$  also generates only free carriers.<sup>37</sup> Therefore, we expect  $\eta_{33} > \eta_{22}$  at low field, and as  $F$  is increased, we expect  $\eta_{33}$  to grow and remain larger than  $\eta_{22}$ .

In conclusion, when photons of energy  $\sim 2E_g$  are absorbed in the intrinsic region of a CNT photodiode, our data suggest it is possible to extract a photocurrent that corresponds to more than one electron per photon. We observed this high-efficiency process by increasing CNT diameter to  $\geq 2.6$  nm, and increasing the axial electric field to  $\geq 10$  V/ $\mu\text{m}$  (a regime of diameter and field that have not been studied previously). Higher energy optical excitation (for example  $S_{33}$  resonant excitation) gives even higher PCQY. The observed diameter dependence of PCQY is consistent with the diameter dependence of exciton binding energy (large diameter CNTs have lower exciton binding energy). Interestingly, increasing diameter is also expected to reduce the rate of impact ionization,<sup>11</sup> however, our experiments suggest there are CNT diameters for which rapid impact ionization can co-exist with exciton dissociation. Possible directions for future work include the use of dielectric environment to tune the strength of the Coulomb interaction in the CNT,<sup>44</sup> so that high-efficiency photocurrent generation could be achieved at lower electric field.

### Supporting Information.

The Supporting Information is available free of charge on the ACS Publications website.

Detailed description of photon flux calculations, the effect of Stark shift and mechanical strain on the  $S_{22}$  exciton peak position, calculations of the exciton resonance oscillator strength and line width as a function of axial electric field, computational methods for self-consistent field calculations, imaging the intrinsic region length, illuminated  $IV$ -curves measured with  $S_{22}$  excitation, details of the CNT growth procedure, and a summary of the data collected on all CNTs discussed in the study.

## Author Information

### Corresponding Author

\*(E.D.M) Email: ethan.minot@oregonstate.edu

### Author Contributions

D.R.M. performed the experiments and analysis of experimental data. M.J.S. performed finite-difference time domain simulations, analyzed computational results and assisted with experiments. A.B. performed self-consistent electrostatics simulations. V.P. calculated the effect of electric field on the CNT absorption spectra and assisted with data analysis. E.D.M. conceived the experiments and contributed to the experimental design and analysis. All authors contributed to the manuscript writing.

### Acknowledgements

This material is based upon work supported by the National Science Foundation under Grant No. 1709800. A portion of device fabrication was carried out in the University of California Santa Barbara (UCSB) nanofabrication facility. Part of this research was conducted at the Northwest Nanotechnology Infrastructure, a National Nanotechnology Coordinated Infrastructure site at Oregon State University which is supported in part by the National Science Foundation (grant ECCS-1542101) and Oregon State University.

### References

- (1) Pandey, A.; Guyot-Sionnest, P. Slow Electron Cooling in Colloidal Quantum Dots. *Science* **2008**, *322*, 929–932.
- (2) Jiao, S.; Shen, Q.; Mora-Seró, I.; Wang, J.; Pan, Z.; Zhao, K.; Kuga, Y.; Zhong, X.; Bisquert, J. Band Engineering in Core/Shell ZnTe/CdSe for Photovoltage and Efficiency Enhancement in Exciplex Quantum Dot Sensitized Solar Cells. *ACS Nano* **2015**, *9*, 908–915.
- (3) Tomić, S.; Miloszewski, J. M.; Tyrrell, E. J.; Binks, D. J. Design of Core/Shell Colloidal Quantum Dots for MEG Solar Cells. *IEEE J. Photovolt.* **2016**, *6*, 179–184.
- (4) Cirloganu, C. M.; Padilha, L. A.; Lin, Q.; Makarov, N. S.; Velizhanin, K. A.; Luo, H.; Robel, I.; Pietryga, J. M.; Klimov, V. I. Enhanced Carrier Multiplication in Engineered Quasi-Type-II Quantum Dots. *Nat. Commun.* **2014**, *5*, 4148.
- (5) Stewart, J. T.; Padilha, L. A.; Qazilbash, M. M.; Pietryga, J. M.; Midgett, A. G.; Luther, J. M.; Beard, M. C.; Nozik, A. J.; Klimov, V. I. Comparison of Carrier Multiplication Yields in PbS and PbSe Nanocrystals: The Role of Competing Energy-Loss Processes. *Nano Lett.* **2012**, *12*, 622–628.

- (6) Davis, N. J. L. K.; Böhm, M. L.; Tabachnyk, M.; Wisnivesky-Rocca-Rivarola, F.; Jellicoe, T. C.; Ducati, C.; Ehrler, B.; Greenham, N. C. Multiple-Exciton Generation in Lead Selenide Nanorod Solar Cells with External Quantum Efficiencies Exceeding 120%. *Nat. Commun.* **2015**, *6*, 8259.
- (7) Semonin, O. E.; Luther, J. M.; Choi, S.; Chen, H.-Y.; Gao, J.; Nozik, A. J.; Beard, M. C. Peak External Photocurrent Quantum Efficiency Exceeding 100% via MEG in a Quantum Dot Solar Cell. *Science* **2011**, *334*, 1530–1533.
- (8) Sambur, J. B.; Novet, T.; Parkinson, B. A. Multiple Exciton Collection in a Sensitized Photovoltaic System. *Science* **2010**, *330*, 63–66.
- (9) Gabor, N. M. Impact Excitation and Electron–Hole Multiplication in Graphene and Carbon Nanotubes. *Acc. Chem. Res.* **2013**, *46*, 1348–1357.
- (10) Chen, J.; Perebeinos, V.; Freitag, M.; Tsang, J.; Fu, Q.; Liu, J.; Avouris, P. Bright Infrared Emission from Electrically Induced Excitons in Carbon Nanotubes. *Science* **2005**, *310*, 1171–1174.
- (11) Perebeinos, V.; Avouris, P. Impact Excitation by Hot Carriers in Carbon Nanotubes. *Phys. Rev. B* **2006**, *74*, 121410.
- (12) Gabor, N. M.; Zhong, Z.; Bosnick, K.; Park, J.; McEuen, P. L. Extremely Efficient Multiple Electron-Hole Pair Generation in Carbon Nanotube Photodiodes. *Science* **2009**, *325*, 1367–1371.
- (13) Wang, S.; Khafizov, M.; Tu, X.; Zheng, M.; Krauss, T. D. Multiple Exciton Generation in Single-Walled Carbon Nanotubes. *Nano Lett.* **2010**, *10*, 2381–2386.
- (14) Barkelid, M.; Steele, G. A.; Zwiller, V. Probing Optical Transitions in Individual Carbon Nanotubes Using Polarized Photocurrent Spectroscopy. *Nano Lett.* **2012**, *12*, 5649–5653.
- (15) Malapanis, A.; Perebeinos, V.; Sinha, D. P.; Comfort, E.; Lee, J. U. Quantum Efficiency and Capture Cross Section of First and Second Excitonic Transitions of Single-Walled Carbon Nanotubes Measured through Photoconductivity. *Nano Lett.* **2013**, *13*, 3531–3538.
- (16) Aspitarte, L.; McCulley, D. R.; Minot, E. D. Photocurrent Quantum Yield in Suspended Carbon Nanotube p–n Junctions. *Nano Lett.* **2016**, *16*, 5589–5593.
- (17) Wang, F.; Wang, S.; Yao, F.; Xu, H.; Wei, N.; Liu, K.; Peng, L.-M. High Conversion Efficiency Carbon Nanotube-Based Barrier-Free Bipolar-Diode Photodetector. *ACS Nano* **2016**, *10*, 9595–9601.
- (18) Kumamoto, Y.; Yoshida, M.; Ishii, A.; Yokoyama, A.; Shimada, T.; Kato, Y. K. Spontaneous Exciton Dissociation in Carbon Nanotubes. *Phys. Rev. Lett.* **2014**, *112*, 117401.
- (19) Perebeinos, V.; Avouris, P. Exciton Ionization, Franz–Keldysh, and Stark Effects in Carbon Nanotubes. *Nano Lett.* **2007**, *7*, 609–613.
- (20) Baer, R.; Rabani, E. Can Impact Excitation Explain Efficient Carrier Multiplication in Carbon Nanotube Photodiodes? *Nano Lett.* **2010**, *10*, 3277–3282.
- (21) Chang, S.-W.; Theiss, J.; Hazra, J.; Aykol, M.; Kapadia, R.; Cronin, S. B. Photocurrent Spectroscopy of Exciton and Free Particle Optical Transitions in Suspended Carbon Nanotube Pn-Junctions. *Appl. Phys. Lett.* **2015**, *107*, 053107.
- (22) Chang, S. W.; Bergemann, K.; Dhall, R.; Zimmerman, J.; Forrest, S.; Cronin, S. B. Nonideal Diode Behavior and Bandgap Renormalization in Carbon Nanotube P-n Junctions. *IEEE Trans. Nanotechnol.* **2014**, *13*, 41–45.
- (23) Ding, L.; Tselev, A.; Wang, J.; Yuan, D.; Chu, H.; McNicholas, T. P.; Li, Y.; Liu, J. Selective Growth of Well-Aligned Semiconducting Single-Walled Carbon Nanotubes. *Nano Lett.* **2009**, *9*, 800–805.
- (24) Aspitarte, L.; McCulley, D. R.; Minot, E. D. A Nanoscale Pn Junction in Series with Tunable Schottky Barriers. *J. Appl. Phys.* **2017**, *122*, 134304.

- (25) Lee, J. U. Photovoltaic Effect in Ideal Carbon Nanotube Diodes. *Appl. Phys. Lett.* **2005**, *87*, 073101.
- (26) Perebeinos, V.; Avouris, P. Phonon and Electronic Nonradiative Decay Mechanisms of Excitons in Carbon Nanotubes. *Phys. Rev. Lett.* **2008**, *101*, 057401.
- (27) Yasukochi, S.; Murai, T.; Moritsubo, S.; Shimada, T.; Chiashi, S.; Maruyama, S.; Kato, Y. K. Gate-Induced Blueshift and Quenching of Photoluminescence in Suspended Single-Walled Carbon Nanotubes. *Phys. Rev. B* **2011**, *84*, 121409.
- (28) DeBorde, T.; Kevek, J. W.; Sharf, T.; Wardini, J. L.; Minot, E. D. A Spectrally-Tunable Photocurrent Microscope for Characterizing Nanoelectronic Devices. *Proc. IEEE Conf. Nanotechnol.* **2011**, 382–386.
- (29) Wang, F.; Dukovic, G.; Brus, L. E.; Heinz, T. F. The Optical Resonances in Carbon Nanotubes Arise from Excitons. *Science* **2005**, *308*, 838–841.
- (30) Liu, K.; Deslippe, J.; Xiao, F.; Capaz, R. B.; Hong, X.; Aloni, S.; Zettl, A.; Wang, W.; Bai, X.; Louie, S. G.; et al. An Atlas of Carbon Nanotube Optical Transitions. *Nat. Nanotechnol.* **2012**, *7*, 325–329.
- (31) DeBorde, T.; Aspitarte, L.; Sharf, T.; Kevek, J. W.; Minot, E. D. Determining the Chiral Index of Semiconducting Carbon Nanotubes Using Photoconductivity Resonances. *J. Phys. Chem. C* **2014**, *118*, 9946–9950.
- (32) Minot, E. D.; Yaish, Y.; Sazonova, V.; Park, J.-Y.; Brink, M.; McEuen, P. L. Tuning Carbon Nanotube Band Gaps with Strain. *Phys. Rev. Lett.* **2003**, *90*, 156401.
- (33) Huang, M.; Wu, Y.; Chandra, B.; Yan, H.; Shan, Y.; Heinz, T. F.; Hone, J. Direct Measurement of Strain-Induced Changes in the Band Structure of Carbon Nanotubes. *Phys. Rev. Lett.* **2008**, *100*, 136803.
- (34) He, X.; Htoon, H.; Doorn, S. K.; Pernice, W. H. P.; Pyatkov, F.; Krupke, R.; Jeantet, A.; Chassagneux, Y.; Voisin, C. Carbon Nanotubes as Emerging Quantum-Light Sources. *Nat. Mater.* **2018**, *17*, 663.
- (35) Liu, K.; Hong, X.; Choi, S.; Jin, C.; Capaz, R. B.; Kim, J.; Wang, W.; Bai, X.; Louie, S. G.; Wang, E.; et al. Systematic Determination of Absolute Absorption Cross-Section of Individual Carbon Nanotubes. *PNAS* **2014**, *111*, 7564–7569.
- (36) Hertel, T.; Perebeinos, V.; Crochet, J.; Arnold, K.; Kappes, M.; Avouris, P. Intersubband Decay of 1-D Exciton Resonances in Carbon Nanotubes. *Nano Lett.* **2008**, *8*, 87–91.
- (37) Steiner, M.; Freitag, M.; Perebeinos, V.; Tsang, J. C.; Small, J. P.; Kinoshita, M.; Yuan, D.; Liu, J.; Avouris, P. Phonon Populations and Electrical Power Dissipation in Carbon Nanotube Transistors. *Nat. Nanotechnol.* **2009**, *4*, 320–324.
- (38) Hofmann, M. S.; Glückert, J. T.; Noé, J.; Bourjau, C.; Dehmel, R.; Högele, A. Bright, Long-Lived and Coherent Excitons in Carbon Nanotube Quantum Dots. *Nat. Nanotechnol.* **2013**, *8*, 502–505.
- (39) Sarpkaya, I.; Zhang, Z.; Walden-Newman, W.; Wang, X.; Hone, J.; Wong, C. W.; Strauf, S. Prolonged Spontaneous Emission and Dephasing of Localized Excitons in Air-Bridged Carbon Nanotubes. *Nat. Commun.* **2013**, *4*, 2152.
- (40) Ishii, A.; Yoshida, M.; Kato, Y. K. Exciton Diffusion, End Quenching, and Exciton-Exciton Annihilation in Individual Air-Suspended Carbon Nanotubes. *Phys. Rev. B* **2015**, *91*, 125427.
- (41) Hertel, T.; Himmelein, S.; Ackermann, T.; Stich, D.; Crochet, J. Diffusion Limited Photoluminescence Quantum Yields in 1-D Semiconductors: Single-Wall Carbon Nanotubes. *ACS Nano* **2010**, *4*, 7161–7168.
- (42) Mohite, A. D.; Gopinath, P.; Shah, H. M.; Alphenaar, B. W. Exciton Dissociation and Stark Effect in the Carbon Nanotube Photocurrent Spectrum. *Nano Lett.* **2008**, *8*, 142–146.

- (43) Dukovic, G.; Wang, F.; Song, D.; Sfeir, M. Y.; Heinz, T. F.; Brus, L. E. Structural Dependence of Excitonic Optical Transitions and Band-Gap Energies in Carbon Nanotubes. *Nano Lett.* **2005**, 5, 2314–2318.
- (44) Aspitarte, L.; McCulley, D. R.; Bertoni, A.; Island, J. O.; Ostermann, M.; Rontani, M.; Steele, G. A.; Minot, E. D. Giant Modulation of the Electronic Band Gap of Carbon Nanotubes by Dielectric Screening. *Sci. Rep.* **2017**, 7, 8828.

TOC Graphic

